WestVirginiaUniversity
THE RESEARCH REPOSITORY @ WVU

Analysis of global and local stress changes in a longwall gateroad

I.B. Tulu

G.S. Esterhuizen

D. Gearhart

T.M. Klemetti

K.M. Mohamed

See next page for additional authors

Authors

I.B. Tulu, G.S. Esterhuizen, D. Gearhart, T.M. Klemetti, K.M. Mohamed, and D.W.H. Su

Analysis of global and local stress changes in a longwall gateroad

I.B. Tulu [a,*], G.S. Esterhuizen [b], D. Gearhart [b], T.M. Klemetti [b], K.M. Mohamed [b], D.W.H. Su [b]

[a] Department of Mining Engineering, West Virginia University, Morgantown 26505, USA
[b] NIOSH, Pittsburgh Mining Research Division, Pittsburgh 15216, USA

ABSTRACT

A numerical-model-based approach was recently developed for estimating the changes in both the horizontal and vertical loading conditions induced by an approaching longwall face. In this approach, a systematic procedure is used to estimate the model's inputs. Shearing along the bedding planes is modeled with ubiquitous joint elements and interface elements. Coal is modeled with a newly developed coal mass model. The response of the gob is calibrated with back analysis of subsidence data and the results of previously published laboratory tests on rock fragments. The model results were verified with the subsidence and stress data recently collected from a longwall mine in the eastern United States.
© 2017 Published by Elsevier B.V. on behalf of China University of Mining & Technology. This is an open access article under the CC BY-NC-ND license (http://creativecommons.org/licenses/by-nc-nd/4.0/).

1. Introduction

In 2015, there were 40 longwall mines operating in the United States, each producing an average of 4.5 million tons of coal per year, and they supplied 60% of the U.S. underground coal production. This represents a substantial increase from 50% over the previous three years [1]. During this period, reportable roof fall rates in U.S. longwall mines also increased. Large roof falls that can block the gateroads are not only a ground-fall hazard; they can disrupt the ventilation system, block the escape ways, and increase the potential for elevated methane levels in the gob. To address these hazards, the National Institute for Occupational Safety and Health (NIOSH) Pittsburgh Mining Research Division (PMRD) is conducting research to improve the design of ground control systems in longwall gateroads.

Gateroad layout is primarily determined by the longwall pillar design. Generally, the required dimensions of the pillars around a longwall panel are determined first, which dictates the location of the gateroads relative to the mined panel. The analysis of longwall pillar stability (ALPS) method is the most accepted design procedure in the United States [2]. The ALPS method accounts for local roof geology in the gateroad stability assessment by including the coal mine roof rating as an input parameter [2]. The key assumption in the ALPS method is that unstable pillars will result in unstable gate entries. However, experience provides examples of mines

where pillar stability and gateroad stability are loosely correlated [3].

Gateroad support design is largely empirical, often based on a trial-and-error approach. Gateroad stability and safety can be improved by introducing an engineering-based design approach that specifically considers the rock mass and support response to changes in both the horizontal and vertical loading conditions induced by the approaching longwall face. Such complex stress changes during a longwall retreat can be evaluated with calibrated numerical models, allowing support systems to be designed that can accommodate the expected loading conditions.

2. Longwall model development and calibration

Esterhuizen et al. developed a modeling approach that can be used to provide realistic stress and deformation results along the gateroad chain pillars [4]. In this approach, an "equivalent element" method is used to capture the stress/strain response of the pillars and the immediate roof and floor rocks to model large-scale, three-dimensional retreat mining layouts. One limitation of this approach is that the response of the immediate roof to horizontal stress change during the retreat mining cannot be investigated because only the vertical stress is solved within the equivalent elements. Recently, this approach has been updated for estimating the changes in both the horizontal and vertical loading conditions in the immediate roof of the gateroads [5]. The modified approach uses standard elements to model the pillars, roof, and floor, which provides the full stress tensor, including horizon-

* Corresponding author.
 E-mail address: itulu@mail.wvu.edu (I.B. Tulu).

tal stress components in the roof of the coal bed. In addition, interface elements are introduced between main geologic units to more accurately model shear and bending of the overburden strata.

2.1. Pillar strength modeling

Recently at NIOSH, Mohamed et al. developed a coal material model. In this model, the peak strength of the coal is evaluated by the generalized Hoek-Brown failure criterion [6–8]. The residual stiffness and strength are evaluated by the Fang and Harrison local degradation model [9]. The dilation of the coal material is defined by the Alejano and Alonso peak-dilation model [9,10].

Mohamed et al. indicated that the Mohr-Coulomb constitutive model provides a method for describing the dilation behavior of rocks, and it is available in the majority of numerical codes [7]. Therefore, in this model, the equivalent Mohr-Coulomb model parameters derived from the Hoek-Brown criterion are used. This model simulates the peak and post-peak behaviors of the coal material by using a strain-softening, ubiquitous joint model available in the FLAC3D software.

The input parameters used for coal in this paper are summarized in Table 1. In Table 1, "σci" is the intact unconfined compressive strength of the coal, and m, s and a are the peak strength scaled parameters of coal. The parameter σc represents peak, and σcr is the residual of the field-scale unconfined compressive strength. Nd is a scaled coal degradation parameter. This degradation parameter is used to reduce the strength and stiffness of the coal from peak values to residual values in the coal model. $\Upsilon pcrit$ is the critical plastic shear strain that controls the rate of material degradation. The strength of the coal material is reduced until plastic shear strain reaches to this critical value. Coal material fracturing is simulated by adding an implicit cohesion-less ubiquitous joint within the material. Fractures are initiated in those elements that have plastic shear strain equal to or greater than the "fracture plastic shear strain" parameter detailed in Table 1. The coal model was originally developed to simulate the stress/strain behavior of coal pillar ribs. This model also simulates the stress/strain behavior of full coal pillars satisfactorily, as demonstrated in Fig. 1.

To compare the stress-strain behavior of the pillars generated with the coal model of Mohamed et al. to results obtained by Esterhuizen et al., numerical models were created in which portions of the roof strata, the coal pillar, and the floor strata were simulated [4,7]. The same boundary conditions and model geometries used by Esterhuizen et al. were modeled [4]. Fig. 1 shows the resulting stress-strain curves obtained from the coal models with different pillar width-to-height ratios. The stress-strain behavior presented in Fig. 1 is similar to the results published by Esterhuizen et al. [4]. The new coal model can simulate the fracture development in coal pillar [7]. Post-peak stress/strain behavior was slightly different. For the width-to-height ratios below 8, the pillars exhibit a strain-softening behavior. For the width-to-height ratios above 8, the pillars exhibit a strain-hardening behavior. The peak pillar strengths simulated by the numerical models are compared with the empirical Bieniawski pillar strength equation in Fig. 2. The results show good agreement between the model calculations and the empirical equation.
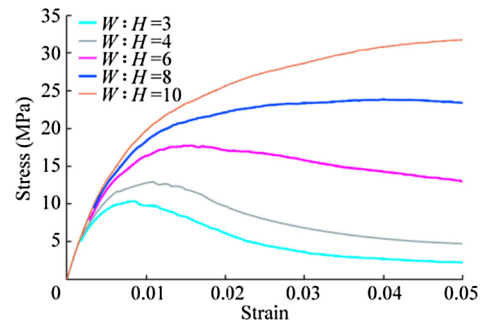

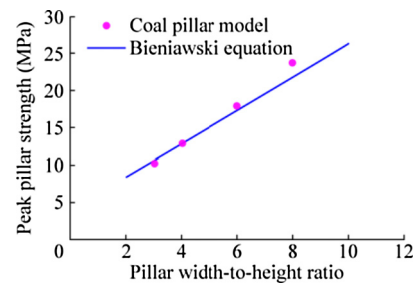**Fig. 1.** Stress-strain curves obtained from a calibrated coal model.

Fig. 2. Pillar strength results obtained by numerical models after calibrating the models to the empirical pillar strength equation.

2.2. Gob response modeling

It is important to simulate the gob response accurately to simulate the load distribution along the gateroad entries. Esterhuizen et al. indicated that gob modeling can follow two approaches: (1) explicitly model the gob formation process so that variations in geology and loading conditions can be studied, (2) implicitly model the gob compaction and load distribution to accurately model load redistribution to gateroad pillars and surrounding rock. As in Esterhuizen et al., the second approach is used in this paper to simulate the behavior of the gob [4].

As indicated by Pappas and Mark, laboratory tests on shale and sandstone fragments showed that the stress-strain response of caved material should follow a strain-hardening curve [11]. Pappas and Mark used the hyperbolic function derived by Salamon to fit test results, and they found that this function sufficiently simulates the strain-hardening gob response [11,12].

$$\sigma = (a \times \varepsilon)/(b - \varepsilon) \tag{1}$$

where σ is the vertical gob stress, MPa; ε the vertical gob strain, and $\varepsilon = b/2$, MPa; b the maximum strain parameter related to void ratio; and a the gob stress.

Esterhuizen et al. calibrated the hyperbolic equation (Eq. (1)) by matching the model results with subsidence profiles that were calculated from the surface deformation prediction software (SDPS) [4,13]. To assist selecting appropriate gob parameters, they followed the same approach used by SDPS, in which the gob is char-

Table 1
Input parameters for coal material.

Elastic property		Strength parameter						Degradation parameter		Ubiquitous joint friction angle	Fracture plastic shear strain
Modulus (GPa)	Poisson's ratio	σci (MPa)	m	s	a	σcr (MPa)	σc (MPa)	Nd	$\Upsilon pcrit$		
3	0.25	20	1.52	0.013	0.5	0.3	2.28	0.503	0.26	25	0.0275

acterized by the ratio of the thicknesses of "strong" and "weak" rocks in the overburden. They classified weak rocks as shales and clay stones that have a field scale uniaxial confining strength (UCS) of less than 40 MPa, while limestone, sandstone, and siltstone have a field scale UCS above 40 MPa and would be classified as strong rocks. Esterhuizen et al. found that 44% represents the maximum vertical strain parameter *b*, which provides the initial bulking factor of 1.79 [4]. They also found four different *a* parameters for four gob types that were classified with a ratio of strong to weak rocks in the overburden: (1) weak (25%), (2) moderate (35%), (3) strong (50%), and (4) very strong (65%). The strong and moderate gob curves derived by Esterhuizen et al. are almost identical to laboratory best-fit curves for sandstone and shale materials that were published by Pappas and Mark [4,11].

Su simulated the behavior of the gob which is assumed to be formed under an initial bulking factor of 1.5 based on observation of caving height in boreholes, representing a maximum vertical strain of 33% and a caving height equal to three times the mining height [14]. Su used this approach very successfully for many years for estimating surface subsidence and pillar stresses for a number of longwall mines [15]. In addition, it was found that the gob parameters used by Su give close stress-strain values to the weak/moderate overburden gob response curves published by Esterhuizen et al. up to a gob compaction of 28% [4,14].

Maximum vertical strain is related to initial bulking factor (or initial void ratio). The average initial bulking factor of the test samples used by Pappas and Mark are: (1) 1.80 for shale, (2) 1.74 for sandstone, and (3) 1.87 for strong sandstone [11]. These values of the bulking factor represent fully rotated and dislocated blocks, which represents the maximum bulking potential of the broken rock. In a mine gob, the void ratio will decrease with distance above the floor [16]. A value of 1.5 appears to be good representation of average bulking factor.

In this paper the gob represents only the caved material and excludes fractured rock above the caved zone. Based on the above discussions and the calibration of the gob response curve with subsidence data, the gob parameters proposed by Esterhuizen et al. were modified by assuming the gob was formed under an average bulking factor of 1.5, which represents a maximum strain of 33% and a caving height equal to three times the mining height measured from the floor [4]. This value of the bulking factor also provides reasonable estimates of the subsidence when used in numerical models. Two values of the *a* parameter are suggested for strong overburden and weak overburden. Fig. 3 shows the stress-strain behavior of these two gob types and a comparison to the tests results of Pappas and Mark [11]. Table 2 shows the gob parameters for these two curves.

In the model, strain-hardening gob behavior is simulated by updating the elastic modulus of each zone with the expected tangent modulus. The expected tangent modulus can be calculated by taking the derivative of Eq. (1) with respect to vertical strain (Eq.
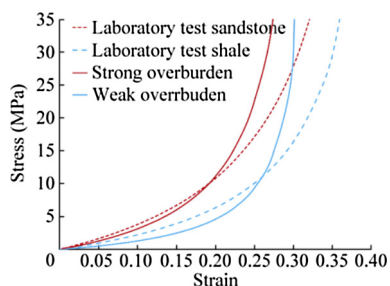

Fig. 3. Stress-strain behavior of the two gob types and a comparison to the tests results.

Table 2
Parameters for modeling various gob types.

Overburden type	*a* (MPa)	*b*
Weak	3.00	0.33
Strong	7.24	0.33

(2)). This task is performed by using the FISH option of the Flac3D software [17].

$$dQ/dQ = E(\varepsilon) = (a \times b)/(b - \varepsilon)^2 \tag{2}$$

2.3. Overburden properties

Esterhuizen et al. published the suggested rock elastic, intact strength and bedding strength properties for modeling large-scale coal measure rock in the United States. Some modifications and corrections were made to the data that was published by Esterhuizen et al. [4]. Updated properties are presented in Tables 3 and 4.

UCS values in Table 3 are laboratory scale values. The field value of the *UCS* is estimated by multiplying the laboratory value with 0.58 [4,8]. Poisson's ratio was set to 0.25. For sandstone and shale, the elastic modulus *E* is estimated from Eq. (3), and for limestone, the elastic modulus is estimated from Eq. (4). These equations were driven from the regression analysis of a large number of *UCS* tests. In Eqs. (3) and (4), the *UCS* is the laboratory scale value in MPa and the resultant elastic modulus is in GPa.

$$E = 0.143 \times UCS + 6.16 \tag{3}$$

$$E = 0.1162 \times UCS + 15.24 \tag{4}$$

The friction angles are determined from the database of tri-axial tests [4]. The friction values are also assumed to be the same in the laboratory and field scales. The cohesion values listed in Table 3 are field scale values and calculated by using Eq. (5).

$$C = \frac{UCS_{field} \times (1 - Sin(\varphi))}{2 \times Cos(\varphi)} \tag{5}$$

where *C* is the field scale cohesion; φ = the friction angle; and $UCS_{field} = UCS_{lab} \times 0.58$.

Tensile strengths σ_t are calculated by using Eq. (6).

$$\sigma_t = 0.1 \times UCS_{field} \tag{6}$$

The bedding strength parameters summarized in Table 4 were derived by Esterhuizen, Mark and Murphy [4]. Bedding tensile strength was set to 10% of the field-scale UCS. Esterhuizen et al. indicated that bedding friction angles may seem to be small compared to small-scale laboratory strength tests, but the presence of weak clay materials, especially in the shale beds, can have a significant impact on the overall shear resistance of a bedding plane [4].

The matrix cohesion and tensile strength decreased from their peak values, given in Table 3, to a residual value of 10% of peak over 5 millistrains of plastic strain [18]. The matrix friction angle remains constant at the values shown in Table 3. The stress-strain behavior of the bedding planes are assumed to be elastic perfectly plastic.

Interfaces between the geological layers in the overburden were modeled with the interface elements. This is the major difference from Esterhuizen et al. [4]. Coulomb's criterion was used to define the limiting shear strength of the interfaces. As described by Su, the coefficient of friction of interfaces was set to 0.25 [14,15]. Joint shear stiffness was set to 0.5 GPa/m, and normal stiffness was set to 10 times the shear stiffness [14,15].

Table 3
Suggested intact rock properties.

Type	UCS (MPa)	E (GPa)	Friction angle (°)	Cohesion (MPa)	Tensile strength (MPa)
Limestone	140	31.51	42	18.08	8.12
	100	26.86	42	12.91	5.80
	80	24.54	40	10.82	4.64
Sandstone	120	23.32	42	15.49	6.96
	100	20.46	40	13.52	5.80
	80	17.60	37	11.57	4.64
	60	14.74	35	9.06	3.48
	40	11.88	30	6.70	2.32
Shale	80	17.60	32	12.86	4.64
	60	14.74	30	10.05	3.48
	40	11.88	25	7.39	2.32
	30	10.45	20	6.09	1.74
	20	9.02	20	4.06	1.16
	10	7.59	20	2.03	0.58
	5	6.88	20	1.02	0.29

Table 4
Suggested bedding strength properties.

Type	Cohesion (MPa)	Friction (°)	Tension (MPa)
Limestone	9.47	32	0.81
	7.55	30	0.58
	6.70	28	0.46
Sandstone	8.11	30	0.70
	6.76	30	0.58
	6.04	27	0.46
	4.53	25	0.35
	3.35	20	0.23
Shale	2.96	10	0.46
	2.44	7	0.35
	1.78	7	0.23
	0.50	7	0.17
	0.30	5	0.12
	0.20	5	0.06
	0.10	5	0.03

3. Verification of the model

Case histories used by Esterhuizen, Mark and Murphy were again used to verify the updated modeling methodology and input parameters [4]. In addition, subsidence and vertical stress data recently collected by the Pittsburgh Mining Research Division (PMRD) from a longwall mine in West Virginia were used to verify the model results. Results of this verification study were published by Tulu et al. [5]. The model verification results showed that the response of coal measure rocks due to longwall mining can be simulated satisfactorily with this updated approach. In this paper, a numerical model is used for estimating the changes in both the horizontal and vertical loading conditions induced by an approaching longwall face in a West Virginia longwall mine.

3.1. Longwall mine panel layout and geology

The geometry of the study sites can be seen in Fig. 4a. The depth of cover throughout the mine ranges from 100 to 230 m, and the typical depth is about 180 m. The longwall panels are roughly 365 m wide by 2200 m long. The gateroad system is a three-entry with approximately center-to-center, 30-m-wide chain pillars. The mining high is approximately 2 m.

Three core holes were drilled between crosscut 42 and 43 in the number 1 entry between Panel #2 and Panel #3 (Fig. 4b and c). One vertical hole was drilled 15 m into the floor, another vertical hole was drilled 15 m into the roof, and a 30° angled hole was drilled 9 m over the pillar and also into the roof. The collar locations for the core holes are at a depth of 182 m. Based on the in-mine mapping, as well as available exploration drillhole data, the geologic conditions are typical for the Allegheny Formation. The Middle Kittanning coal bed that is mined is overlain by dark gray to carbonaceous clay shale. The clay shale grades upward to gray sandy shale, dark gray sandy shale, or gray sandstone. The gray sandy silt shale and dark gray sandy silt shale beds vary in grain size and sand content, based on their proximity to the laterally correlative gray sandstone beds. Grain size and sand content will decrease as distance from the correlative sandstone beds increases [19].

3.2. Field measurements

There were three hollow inclusion cells installed over the panel and three installed over the pillar. The holes for the hollow inclusion cells, from outby to inby, were at 30°, 45°, and 60° from the horizontal, and each hole was 9 m deep (Fig. 4c). The hollow inclusion (HI) cell in the 30° hole over the panel was overcored two times to get the in situ stress in the rock before either panel had mined passed. Table 5 summarizes the measured principal in situ stresses. Details of this instrumentation study were published by Gearhart et al. [20]. In this paper, the stress changes measured by the hollow inclusion cells were compared to model calculations.

4. Three dimensional model development

The overburden in this mine consists of alternating layers of shale, sandstone, and limestone. Fig. 5 shows a portion of the over-
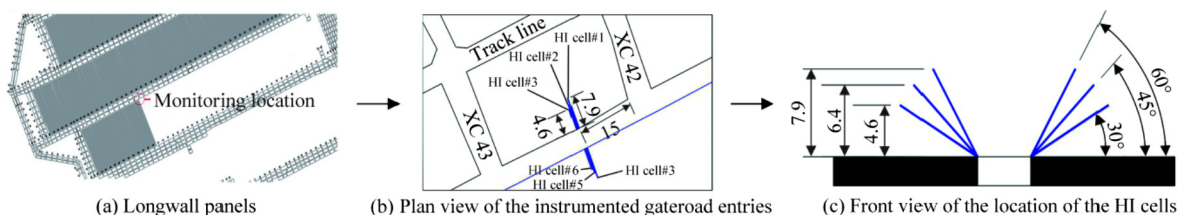

Fig. 4. Field monitoring location.

(a) Longwall panels

(b) Plan view of the instrumented gateroad entries

(c) Front view of the location of the HI cells

Table 5
HI-cell overcoring 3D in situ measurements.

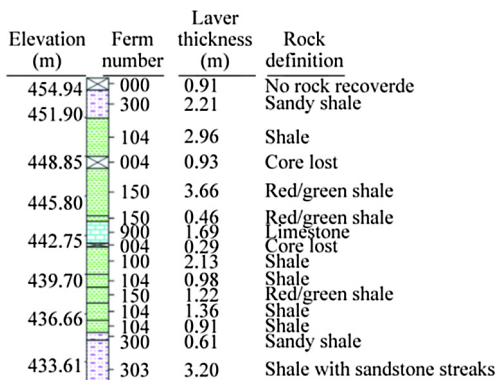| Overcore no.	Principal stress (MPa)			Maximum principal stress direction	
	Maximum	Intermediate	Minimum	Dip (°)	Azimuth (°)
1	6.52	5.47	4.14	13	117
2	8.28	6.58	3.47	4	290

Fig. 5. A portion of the overburden log.

burden log. Because there is not available laboratory test data for mechanical properties of rock layers, Ferm numbers detailed on the geological log were used to assign the approximate mechanical properties for each layer. Molinda and Mark published the point load strength data for common coal measure rocks [21]. Table 6 shows data published by Molinda and Mark who classified each rock type with Ferm numbers [21]. The mechanical properties of each layer are assigned as shown in Tables 3 and 4 by matching the Ferm number from the core log and data published by Molinda and Mark [21].

The thickness weighted average of the laboratory-scale UCS of the overburden is 54 MPa. The behavior of the gob, which is assumed to be formed under an initial bulking factor of 1.5, was simulated with the weak overburden strain-hardening gob parameters detailed in Table 2. The coal material is simulated with the material properties detailed in Table 1. In developing the three-dimensional panel scale model, two initial pseudo 2D models were developed using FLAC3D to investigate the effect of element size on the results. The first pseudo 2D model was developed using 61 different layers with thicknesses ranging from 1 to 10 m that were used to simulate the overburden. Element size in this model was 1 m. The second pseudo 2D model was developed using the same stratigraphy with element sizes ranging from 1 to 10 m to reduce the number of elements in the model. Once both pseudo 2D models were developed, the subsidence and stresses were compared (Figs. 6 and 7). They were found to be similar enough to use the second pseudo model overburden geometry with larger element sizes in the full three-dimensional model. Fig. 6 shows the comparison of the subsidence results calculated by the two pseudo

Table 6
Common coal measure roof rocks and their point load strength properties [21].

| Ferm no.	Description	Axial strength (MPa)	Diametric strength (MPa)			Anisotropy	State	UR
		Average	Std.	Average	Std.			
14	Slumped sandy shale						PA	35
20	Coal	11	2	6	2	1.96	WY, PA, KY, WV	35
113	Black shale with coal streaks	34	7	5	2	6.30	OH, PA	35
114	Black shale	44	30	10	6	4.40	IL, PA	39
119	Black shale with fossil shells	18	6	9	4	2.05	KY	39
122	Dark gray layered shale	53	19	25	31	2.12	WV, PA	45
123	Dark gray shale with coal streaks	36	9	9	4	4.00	PA, WV, OH	33
124	Dark gray shale	36	28	8	4	4.50	PA, WY, KY	36
127	Dark gray fireclay	0	0	9	6		PA, OH, WV	30
137	Light gray green fireclay	33	45	6	0	5.50	KY	28
147	Green claystone	0	0	0	0		OH, PA	30
237	Light gray green fireclay with limestone Nodules	64	24	24	0	2.67	PA	
322	Dark gray shale and Interbedded sandstone	78	27	17	9	4.59	WV, PA	48
323	Dark gray shale with sandstone streaks	48	24	11	5	4.36	PA, KY	40
324	Dark gray massive sandy shale	55	15	9	7	5.91	WV, PA, IL, KY	47
325	Dark gray massive churned sandy shale	42	11	13	11	3.23	WV, PA	48
327	Dark gray sandy fireclay	9	1	0	0		KY	29
332	Light gray green shale and Interbedded sandstone	32	10	10	6	3.20	IL, WY, KY	44
337	Light gray green sandy fire clay	41	8	39	30	1.05		
357	Red and green sandy claystone	64	43	0	0			
437	Red and green sandy fireclay with limestone	12	4	5	2	2.45		
541	Gray crossbedded sandstone	61	5	24	13	2.49	PA, KY, WY	63
543	Gray sandstone with Shale Streaks ripple	80	48	28	14	2.86	OH, PA, WY, KY, WV	63
544	Gray massive sandstone	75	27	94	40	0.80	WV, KY, PA	77
749	Gray sandstone with coal spars	0	0	0	0		WV, OH	43
764	Hard quartz pebble conglomerate	98	23	67	35	1.46	PA	46
772	Shale breccia	22	2	0	0			
782	Shale pebble shaley limestone breccia	0	0	0	0		KY	78
802	Layered fine grained shaley limestone	79	14	15	4	5.27	OH	63
804	Massive fine grained shaley limestone	61	32	41	30			
894	Massive fine grained shaley limestone	30	16	14	3	2.14	KY	35
904	Massive fine grained sandstone	125	38	126	23	0.99	OH	100
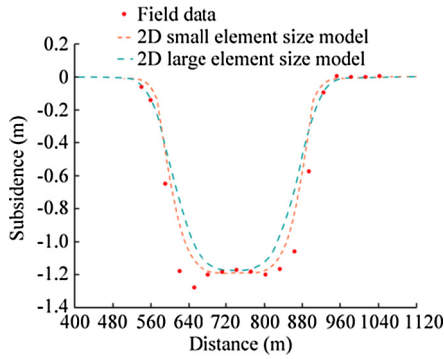
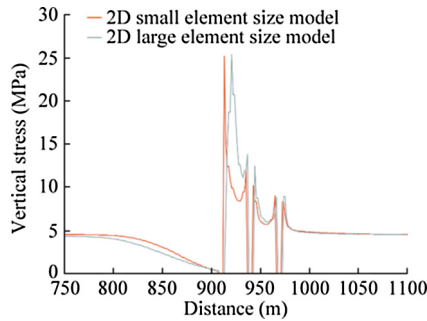**Fig. 6.** Comparison of the subsidence measurements with model results.

Fig. 7. Model-calculated vertical stress distribution.

models and the field data. The model simulates the subsidence at the centerline of the panel within 2% to the field measurements. The shape of the subsidence curve is also satisfactory. The accuracy of the model-calculated subsidence at the centerline of the panel confirms that the model simulates the gob compaction satisfactorily for this case study.

4.1. Comparison of the model results with field measurements and discussions

Horizontal and vertical stresses measured by the HI cells and calculated by the model were compared. Model results were queried at the same location as that of the HI cells relative to the entry, the geology, and the longwall face position. Both sets of HI cells on the pillar side and panel side gave credible results. In this paper, only the results of HI cells installed on the pillar side of the entry at 30°, 45°, and 60° from horizontal were compared with the model results to prevent repetition of the similar results gathered from the panel side. The horizontal stress response measured by the HI cells installed on the pillar side of the entry at 45° and 60° from horizontal are presented as averaged values because the response of these cells was similar but different from the HI cell installed at 30° from horizontal. Vertical stress measured by all of the HI cells are averaged because they all behaved similarly.

4.1.1. Results for 30° HI cell during first panel passing

Fig. 8 shows the comparison of the horizontal stress response measured by the HI cell installed on the pillar side of the entry at 30° from horizontal and calculated by the model during first panel mining. The horizontal axis shows the relative distance between the instrumentation site and longwall face. Positive numbers indicate that the longwall face is outby the instrumented site. The vertical axis shows the percentage of stress change calculated
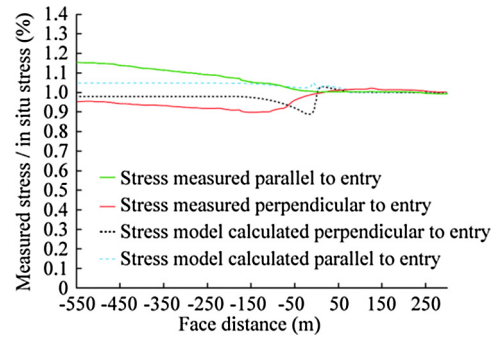

Fig. 8. Horizontal stress response of 30° HI cell during first panel mining.

with respect to the initial in situ stress value of the measured and/or calculated stress component. Solid green and red lines in Fig. 8 show the results for the HI cell. The red line represents the stress measured perpendicular to the entry, and the green line represents the stress measured parallel to the entry. Dotted blue and black lines show the model results.

When the first panel passes by the HI cell location, the magnitude of the horizontal stress perpendicular to the entry direction starts to decrease until it reaches to a value 10% less than its original magnitude. This minimum value was measured when the HI cell was 120 m inby the face. After that, its magnitude increases gradually as far as face is 550 m away from the HI cell. Fig. 8 shows that the model result for the horizontal stress perpendicular to the entry is also showing an initial 10% decrease in the magnitude, followed by an increase. However, the minimum value is calculated approximately 30 m inby the face, and the magnitude increases within 150 m and stays constant.

Fig. 8 shows that the magnitude of the horizontal stress parallel to the entry direction starts to increase gradually as the face approaches and passes the cell location. The model result for the horizontal stress parallel to the entry is also showing a similar increasing trend as shown by the measurement, but the final change in the magnitude calculated by the model is smaller than this measurement.

The reason for the difference in the results appears to be related to the time-dependent response of the rock mass, which means that stress change happens with time and is not solely based on the location of the advancing longwall face. However, the model results are calculated with a static solution, therefore, time-dependent effects are not simulated. Model results only depend on the distance between the face and the monitoring instruments.

4.1.2. Results for the 45° and 60° HI cells during first panel passing

Fig. 9 shows the average change in horizontal stresses measured by two HI cells, installed on the pillar side of the entry at 45° and
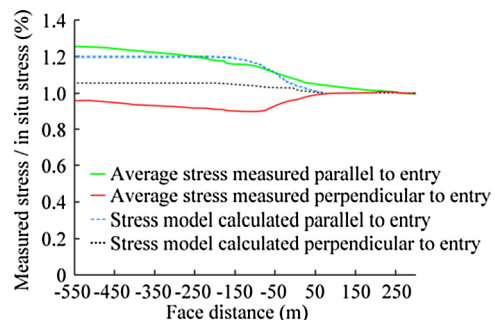

Fig. 9. Average horizontal stress response of 45 and 60° HI cells during first panel mining.

60° from horizontal (Fig.4), and comparable model results. The HI cell measurements follow similar trends as in Fig. 8. The magnitude of horizontal stress change calculated by the model parallel to the entry is approximately 20% of the in situ value, which is similar to the field measurement. However, the model calculates a gradual increase in horizontal stress perpendicular to the entry, which contradicts with the field measurement.

The difference in the stress magnitude perpendicular to the entry may be related to the fact that the geology of the roof in the model consists of uniform strata over the entire longwall panel. However, the geological model developed from the core-hole data showed that the thickness of each stratum can change rapidly and strata are not uniform. There is a strong limestone stratum on the roof which is very close to the HI cells, and its thickness and height from the roof can vary within a distance of 10 m, based on the core-hole data obtained at the monitoring site. The core-hole data over the extent of the longwall panel is too widely spaced to identify local variations of the limestone bed. The difference between the uniform geology in the model and the actual geology might create the difference between the model results and HI cells measurements.

4.1.3. Results for vertical stress changes during first panel passing

Fig. 10 shows the average vertical stresses measured by three HI cells, installed on the pillar side of the entry at 30°, 45°, and 60° from horizontal and comparable model results. Vertical stress measured by the HI cells increased by 44% of its initial value. The vertical stress measured by the HI cells started to increase when the face was approximately 180 m inby the HI cells and continued to increase until the face was 480 m outby the HI cells. Vertical stress calculated by the model increased by 32% of its initial value. Model results showed that vertical stress started to increase when the face was approximately 30 m inby the HI cells and continued to increase until the face was 120 m outby the measurement location.

The difference between the vertical stress measurements and model results appears to be related to the time-dependent response of the rock mass measured by the HI cells, but not included in the model. However, the magnitude and general trend of the vertical stress predicted by the model is similar to the field measurements.

4.1.4. Results for 30° HI cell during second panel passing

Fig. 11 shows the comparison of the horizontal stress response measured by the HI cell installed on the pillar 30° from horizontal and calculated by the model during the second panel mining. Both horizontal stresses measured by the HI cell stayed constant until the face is near the HI cell. After that, the horizontal stress parallel to the entry started to increase and, perpendicular to entry, started to decrease. The model results also showed similar trends. However, the model results showed a gradual increase of horizontal
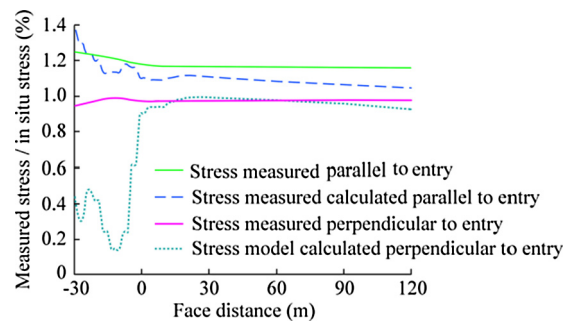

Fig. 11. Horizontal stress response of 30° HI cell during second panel mining.

stresses when the instrument location was outby the face. In addition, when the face was near the instrumented location, horizontal stresses parallel to entry started to increase with a higher slope than the measurement. Similarly, horizontal stress perpendicular to the entry started to drop with a higher slope than measured.

In this case, the model calculated horizontal stress changes that were again more rapid as compared to HI cell measurements. The HI cells indicated that there is a delayed response of the rock mass to changes in the longwall face position. Time-dependent behavior is not included in the models. The model response only depends on the relative location of the cells with respect to the longwall face.

4.1.5. Results for 45° and 60° HI cells during second panel passing

Fig. 12 shows the comparison of the average horizontal stress response measured by the HI cells installed on the pillar 45° and 60° from horizontal and calculated by the model during the second panel mining. Both horizontal stresses measured by the HI cells stayed constant until the face is near the monitoring instruments. After that, both stresses started to increase. The model results showed a gradual increase compared to measurements for stress calculated perpendicular to the entry. The stress calculated parallel to the entry decreased gradually from its peak when the instruments' location is inby the face.

There was a significant difference between the measured and model results for the horizontal stress perpendicular to the entry after the panel had passed the instrument site. The difference may be related to the slower time-dependent response of the rock mass compared to the instantaneous response of the model. A further contributing factor may be the difference between the uniform geology assumed in the model and the effect of unknown variations in the actual geology.

4.1.6. Average results for vertical stress during second panel passing

Fig. 13 shows the comparison of the average vertical stress response measured by the HI cells installed on the pillar at 30°,
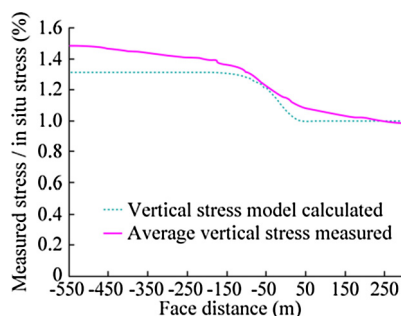

Fig. 10. Average vertical stresses response by three HI cells during first panel mining.
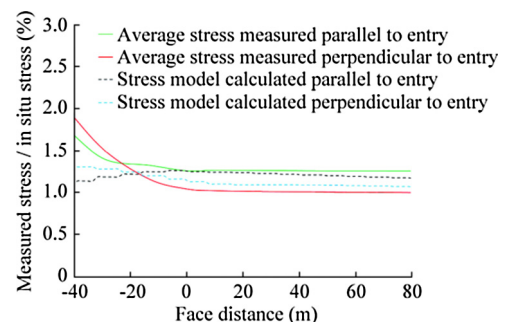

Fig. 12. Average horizontal stress response of 45° and 60° HI cells during second panel mining.
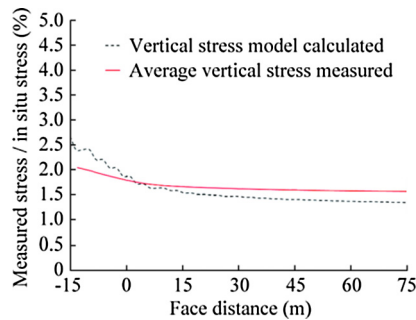
Fig. 13. Average vertical stress response by three HI cells during second panel mining.

45°, and 60° from horizontal and calculated by the model during the second panel mining. The vertical stress measured by the HI cells increased more than 2 times of its initial value when the face is approximately 15 m outby the HI cells. Vertical stress calculated by the model increased 2.5 times of its initial value at the same point.

4.2. Discussion

During the first panel mining, the HI cell data showed that the horizontal stress perpendicular to the entry reduced from its original value, and the horizontal stress measured parallel to the entry increased. The model results also captured this behavior. This means that after the first panel passed, the stress was oriented in a more favorable direction with respect to the entries and in a less favorable direction for the crosscuts.

During the second panel mining, the horizontal stress that measured parallel to the entry started to increase and that perpendicular to entry started to decrease. This means that after the second panel passed, the stress was oriented in an even more favorable direction with respect to the entries compared to the situation after passing of the first panel.

The HI-cell measurements also provided some insight into the height of the caved zone over the longwall panel. The average horizontal stresses measured by the HI cells installed at 45° and 60° over the pillar started to increase as the face passed the instruments. The horizontal stress perpendicular to the entry increased more than the horizontal stress parallel to entry. The 30° cell did not indicate a similar change in stress. This response can be explained if the HI cells are located above the stress shadow of the caved zone, and stress is transferred to the upper strata that has not caved yet. It, therefore, appears to indicate that the height of caving was between 4.5 and 6 m above the roof line, which verifies that the bulking factor of 1.5 is a good approximation for modeling the height of the caved rock.

5. Conclusions

This paper summarizes and verifies an updated approach for panel scale modeling of longwall extraction with subsidence/stress data recently collected from a longwall mine in the eastern United States. The model results show that the response of coal measure rocks due to longwall mining can be simulated satisfactorily with this updated approach. The paper also provides a basic set of input data and a modeling approach for overburden rocks, coal material, and gob material.

There are some differences between the measurements and model results. The HI cell measurements demonstrated that there is a delayed, time-dependent response of the rock mass to changes in the mining geometry. However, the model did not include time-

dependent effects. The results are calculated with a static solution that assumes instantaneous response of the rock mass to changes in the mining geometry. The model results are only dependent on the relative distance between the face and the instruments. In addition, the model assumes uniform geology over the longwall panels, but in reality the geology of the roof can change over short distances. The spacing of the core holes is insufficient to identify these local changes in geology. These differences between the real world and the model approximation are likely to have contributed to the difference between the model results and HI cell measurements.

During the first panel mining, the measurements and model results showed that the horizontal stress measured perpendicular to the entry reduced from its original value and the horizontal stress measured parallel to the entry increased. This means that, after the first panel passed, the stress was oriented in a more favorable direction with respect to the entries, and less favorable for the crosscuts. During the second panel mining, measurement and model results showed that the stress was oriented in an even more favorable direction with respect to entries compared to the situation after passing of the first panel.

The elevated horizontal stress measured inby the face by the 45° and 60° HI cells appeared to indicate that the height of the caved zone extended less than 4.5 m above the roof line. This observation seems to confirm that the bulking factor of 1.5 is a reasonable value for estimating the height of the caved zone.

Disclaimer

The findings and conclusions in this report are those of the authors and do not necessarily represent the views of the National Institute for Occupational Safety and Health (NIOSH). Mention of any company name, product, or software does not constitute endorsement by NIOSH.

References

[1] Sears MM, Tulu IB, Esterhuizen GS. Overview of Current Longwall gateroad support practices. In: Proceedings of the society for, mining, metallurgy and exploration, inc., annual conference, Denver, Colorado.

[2] Mark C. Analysis of longwall pillar stability (ALPS): an update. In: Proceedings of the workshop on coal pillar mechanics and design. Bureau of Mines IC 9315; 1992. p. 238–49.

[3] Su DWH, Draskovich DJ, Thomas EP. Pillar design and roof support for controlling longwall headgate subject to high horizontal stresses. In: Proceedings of the 22nd international conference on ground control in mining, Morgantown, 25–27 July 2003. p. 1–10.

[4] Esterhuizen GS, Mark C, Murphy MM. Numerical model calibration for simulating coal pillars, gob and overburden response. In: Proceedings of the 29th international conference on ground control in mining, Morgantown, 25–27 July 2010. p. 1–12.

[5] Tulu IB, Esterhuizen GS, Mohamed KM, Klemetti TM. Verification of a calibrated longwall model with field measurements. In: 51st US rock mechanics/geomechanics symposium. American Rock Mechanics Association; 2017.

[6] Mohamed KM, Tulu IB, Klemetti T. Numerical simulation of deformation and failure process of coal-mass. In: 49th US rock mechanics/geomechanics symposium. American Rock Mechanics Association; 2015.

[7] Mohamed KM, Tulu IB, Murphy MM. Numerical model calibration for simulating coal ribs. In: Proceedings of the society for, mining, metallurgy and exploration, inc., annual conference, Phoenix, Arizona.

[8] Hoek E, Brown ET. Underground excavations in rock. London: Inst. Min. Metallurgy; 1980. p. 527.

[9] Fang Z, Harrison JP. Development of a local degradation approach to the modeling of brittle fracture of heterogeneous rocks. Int J Rock Mech Min 2002;39:443–57.

[10] Alejano LR, Alonso E. Considerations of the dilatancy angle in rocks and rock masses. Int J Rock Mech Min 2005;42(4):481–507.

[11] Pappas DM, Mark C. Behavior of simulated gob material. U.S. Bureau of Mines; 1993. RI 9458.

[12] Salamon MDG. Mechanism of caving in longwall coal mining. In: Proceedings of the 21th U.S. rock mechanics symposium, Denver CO. A.A. Balkema; 1990. p. 161–8.

[13] Newman DA, Agioutantis Z, Karmis M. SDPS for windows: an integrated approach to ground deformation prediction. In: Proceedings of the 20th international conference on ground control in mining, Morgantown, 25–27 July 2001. p. 157–62.

[14] Su DWH. Finite Element Modeling of Subsidence induced by underground coal mining: the influence of material nonlinearity and shearing along existing planes of weakness. In: Proceedings of the 10th international conference on ground control in mining, Morgantown, 25–27 July 1991. p. 287–300.

[15] Su DWH. Personal communications; 2016.

[16] Esterhuizen GS, Karacan C. A methodology for determining gob permeability distributions and its application to reservoir modeling of coal mine longwalls. In: Proceedings of the society for, mining, metallurgy and exploration, inc., annual conference, Denver, Colorado.

[17] Itasca Consulting Group. Flac3D User's Guide, Version 5.01, Minnesota; 2003.

[18] Zipf RK. Numerical modeling procedures for practical coal mine design. Proceedings of the international workshop on rock mass classification in underground mine design, NIOSH IC 2007;9498:153–62.

[19] Slaker B, Murphy M, Iannacchione N. Report on geological and mechanical properties of B-UP, B-DOWN, and P30. PMRD internal report, Pittsburgh, PA; 2016. p. 50.

[20] Gearhart D, Esterhuizen G, Tulu IB. In: Proceedings of the 36th international conference on ground control in mining, Morgantown, 24–27 July 2017.

[21] Molinda GM, Mark C. Rating the strength of coal mine roof rocks. Rock mechanics tools and techniques: in proceedings of the 2nd North American rock mechanics symposium: NARMS'96, a regional conference of ISRM, Montréal, Québec, Canada, 19–21 June 1996, vol. 1. US: Taylor & Francis; 1996. p. 413.